ACSNANO www.acsnano.org

ARTICLE

Versatile Transfer of an Ultralong and Seamless Nanowire Array Crystallized at High Temperature for Use in High-Performance Flexible Devices

Min-Ho Seo,[†] Jae-Young Yoo,[†] So-Young Choi,[†,∥] Jae-Shin Lee,[†] Kwang-Wook Choi,[†] Chang Kyu Jeong,[‡] Keon Jae Lee,[§] and Jun-Bo Yoon*[,†]

[†]School of Electrical Engineering, [‡]KAIST Institute for NanoCentury, and [§]Department of Materials Science and Engineering, Korea Advanced Institute of Science and Technology (KAIST), 291 Daehak-ro, Yuseong-gu, Daejeon 34141, Republic of Korea

Supporting Information

ABSTRACT: Nanowire (NW) transfer technology has provided promising strategies to realize future flexible materials and electronics. Using this technology, geometrically controlled, high-quality NW arrays can now be obtained easily on various flexible substrates with high throughput. However, it is still challenging to extend this technology to a wide range of high-performance device applications because its limited temperature tolerance precludes the use of high-temperature annealing, which is essential for NW crystallization and functionalization. A pulsed laser technique has been developed to anneal NWs in the presence of a flexible substrate; however, the induced temperature is not high enough to improve the properties of materials such as ceramics and semiconductors. Here, we present a versatile nanotransfer method that is applicable to NWs that require high-temperature annealing. To successfully anneal NWs during their transfer, the developed fabrication method involves sequential removal of a nanoscale sacrificial layer. Using this method, we first produce an ultralong, perfectly aligned polycrystalline barium titanate ($BaTiO_3$) NW array that is heat treated at 700 °C on a flexible polyethylene terephthalate (PET) substrate. This high-quality piezoelectric NW array on a flexible substrate is used as a flexible nanogenerator that generates current and voltage 37 and 10 times higher, respectively, than those of a nanogenerator made of noncrystallized $BaTiO_3$ NWs.

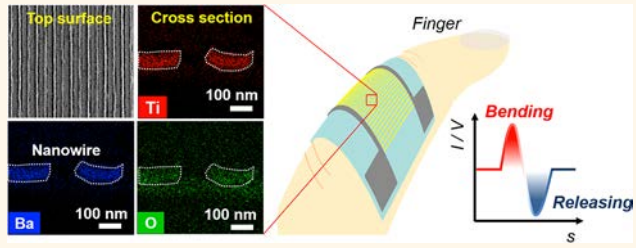

KEYWORDS: *nanowire array, transfer, crystallization, high alignment, flexible piezoelectric*

Nanowires (NWs) on flexible substrates are highly sought after because of their desirable physical and chemical properties[1] for future electronics including artificial skin,[2] multifunctional electrodes,[3] biocompatible sensors,[4] displays,[5] optical,[6] and power[7] applications. To achieve high device performance, it is very important to control the geometry,[8] composition,[9] crystallinity,[10] and defect density[11] of NW arrays on flexible substrates. In addition, recent applications of NW arrays require low-cost fabrication of highly aligned NW arrays defined at specific locations over large areas without any imperfections such as defects, NW loss, or seams.[12,13] Therefore, fabrication of highly ordered, ultralong, and flexible NW arrays on a wide range of large-area functional materials is required to meet the demands of high-performance flexible applications.[14]

Among various emerging nanofabrication processes, transfer methods have received considerable attention because of their promising ability to produce various geometry-controlled NW materials on flexible substrates.[15,16] For example, highly ordered lead zirconate titanate[15] and silicon (Si)[16] NW arrays have been transferred onto flexible substrates by removing the hard substrate. However, this method requires complicated NW patterning and cost-inefficient substrate-removal processes. Other transfer methods such as nanotransfer printing[17] and direct contact transfer[18] have also been developed. Highly aligned NW arrays can be formed on reusable nanograting molds through simple deposition, and then the NWs are transferred from the mold onto a flexible substrate *via* an adhesion-controlled direct contact mechanism.[17] Despite their simplicity and cost-effectiveness, these methods are challenging to use in a wide range of NW applications because of several problems: (i) Material limitations. Deposited NWs, especially

Received: October 11, 2016
Accepted: January 30, 2017
Published: January 30, 2017

DOI: 10.1021/acsnano.6b06842
ACS Nano 2017, 11, 1520–1529

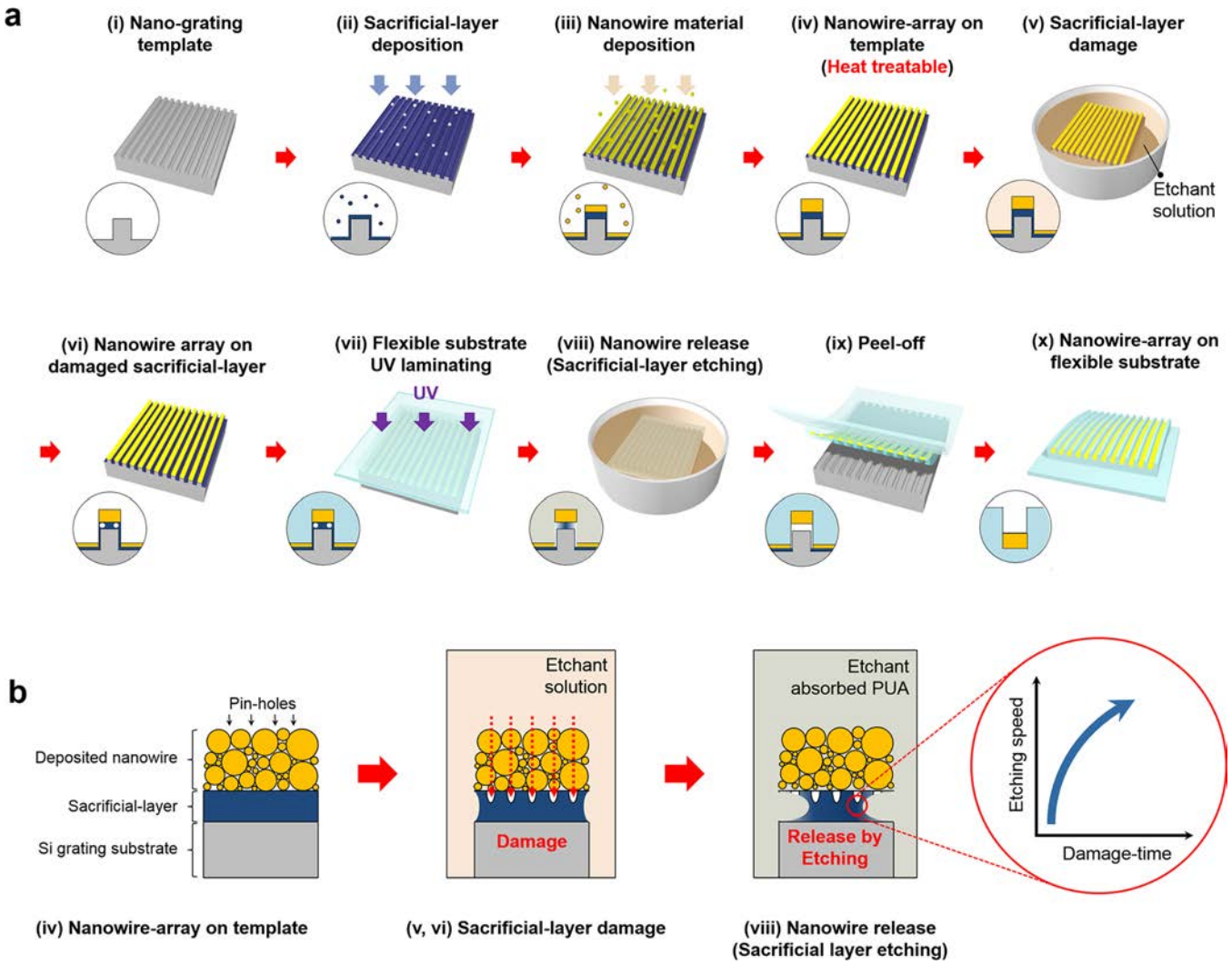

Figure 1. (a) Schematic diagram to fabricate the ultralong, seamless, and perfectly aligned NW array on a flexible substrate by the proposed T-SET process. (Optionally, heat-treatment is possible to enhance crystalline-structure of the NW.) (b) Schematic illustrations of sacrificial layer porosity development by the damage process. Developed porosity raises etching speed by means of a fast etchant-solution diffusion.

semiconductors and ceramics, require high-temperature heat treatment (hundreds of degrees Celsius) to improve their crystallinity and functionality.[19] However, high-temperature heat treatment can degrade nanograting molds[20] or induce strong binding between the NWs and mold,[21] hindering successful transfer. (ii) NW length and domain limitations. It is very difficult to fabricate seamless and large-area nanograting molds with extremely high aspect ratios using general techniques,[22,23] such as high-resolution lithography (KrF, electron beam) and block copolymer self-assembly, because it is challenging to realize large-area, high-throughput nano-patterning in a finely controlled manner.

Recently, we developed a seamless wafer-scale periodic nanograting substrate with an extremely high aspect ratio (4000000:1) using conventional optical lithography and pattern-recovery technology with multiscale spacers,[5] and ultralong, highly aligned NW arrays were fabricated on large-area flexible substrates using the developed substrate. Despite the progress demonstrated by this nanograting master mold, it is still challenging to fabricate ultralong NW arrays composed of various materials on flexible substrates because of their limited temperature tolerance, which means the available material selection range is very narrow.

Herein, we report a fabrication method to transfer ultralong, seamless, and perfectly aligned NW arrays that includes thermal annealing at high temperature (700 °C) during the transfer process. Such high-temperature treatment is allowed by a developed two-step sacrificial-layer etching technique (T-SET). The first etching step generates a physically porous sacrificial layer between the NWs and Si master mold (defined as the damage process), while the second sacrificial layer removal step leads to NWs transfer onto a flexible template from the master mold (defined as the release process). The presence of the sacrificial layer allows high-temperature heat treatment to be conducted during the transfer without any mold degradation and adhesion issues. In this paper, we show that the proposed T-SET process enables the successful transfer of perfectly aligned, ultralong gold (Au) NW arrays using a chromium (Cr) sacrificial layer, onto flexible plastic substrates. Moreover, we also transfer a polycrystalline barium titanate ($BaTiO_3$) ferroelectric ceramic NW array treated at high temperature (700 °C), using a Cr sacrificial layer, onto a flexible plastic substrate. This demonstrates that the method facilitates NWs

DOI: 10.1021/acsnano.6b06842
ACS Nano 2017, 11, 1520–1529

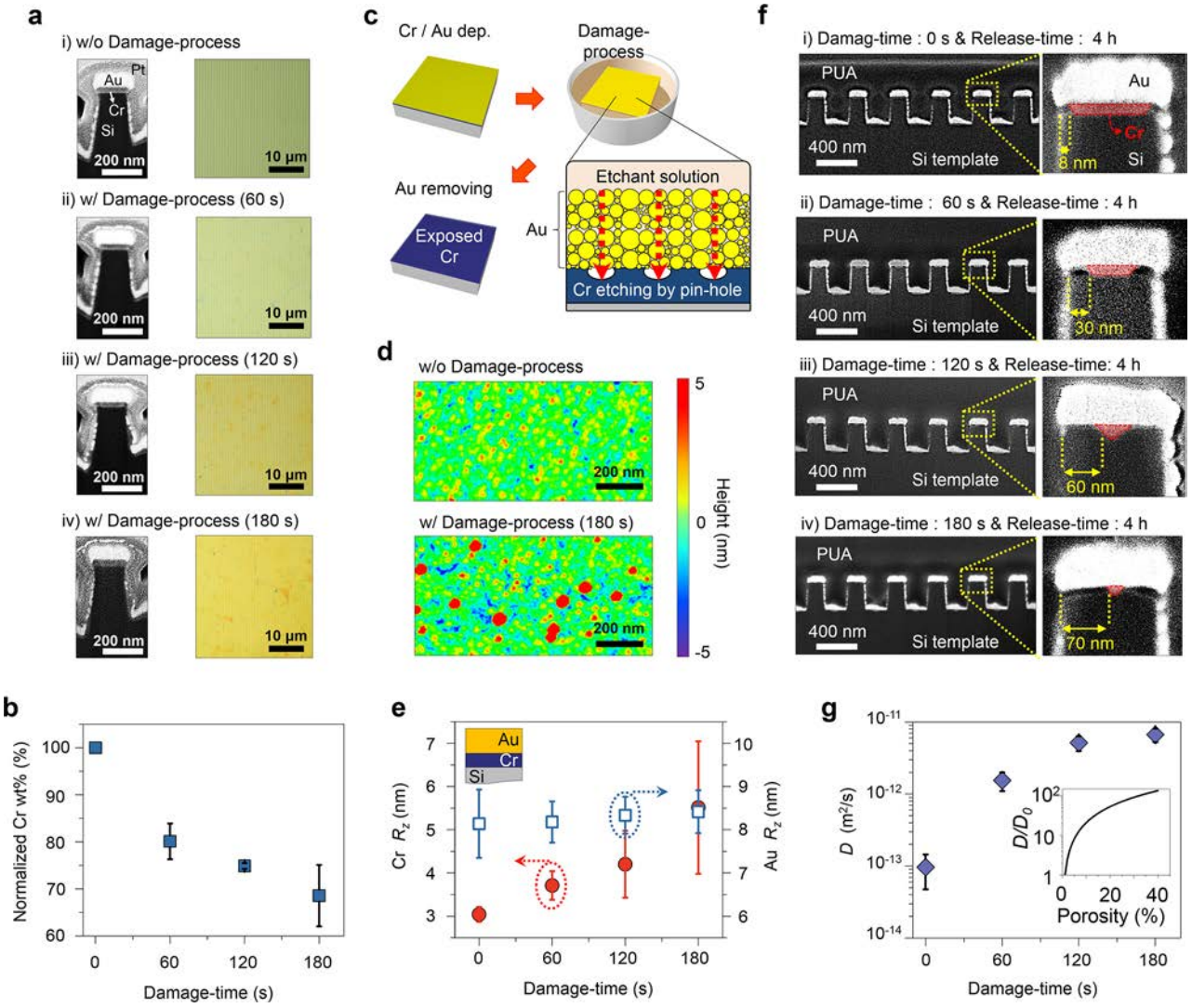

Figure 2. (a) SEM (left-panel) and optical (right-panel) images treated with "damage-process" for (i) 0, (ii) 60, (iii) 120, and (iv) 180 s, respectively. (b) Cr sacrificial layer wt % changes with respect to the damage time. (c) Schematic illustration of the sample preparation to confirm Cr sacrificial layer roughness change by the "damage process". (d) Measured Cr morphology by AFM. Upper and lower data show Cr morphology before and after damage process (180 s), respectively. (e) Measured 10-point average roughness (R_z) change of Au (blue open squares) and Cr (red solid circles) by increasing the damage time. (f) Cross-sectional SEM images of the PUA covered samples after the release process. The magnified sacrificial-layer sections are shown in the right panels. The sacrificial layer was etched more by the longer damage process. The etched distance is shown with a yellow arrow and the remaining Cr is indicated with a red shadow. (g) Diffusion coefficient (D) changes with respect to the "damage time". Inset shows normalized theoretical diffusion coefficient changes (D/D_0) by medium porosity.

transfer with thermal-processed functionalization. Finally, we use the $BaTiO_3$ NW array on the flexible substrate to fabricate a piezoelectric flexible nanogenerator that produces output-enhanced electrical signals from biomechanical energy, which is enabled by the high crystallinity of the heat-treated $BaTiO_3$ NW array.

RESULTS AND DISCUSSION

Figure 1a outlines the proposed T-SET process. First, a sacrificial layer and NWs were sequentially deposited on a Si nanograting master mold, which was fabricated by the multistep process involving spacer lithography and pattern recovery, as described in our previous report (Figure 1a (i–iv)).[5] The sacrificial layer was only under tens of nm thick to prevent distortion of the original master-mold morphology. The proposed damage process is conducted on the specimen after NWs formation (Figure 1a (v, vi)). Then, a flexible template was deposited on the NWs formed in the master mold using a UV-curable polymer resin (Figure 1a (vii)). Finally, the NW array was transferred onto the flexible substrate by removal of the sacrificial layer by a two-step process (Figure 1a (viii–x)). It should be noted that the NW array formed on the hard master mold can be thermally treated at high temperature (Figure 1a (iv)) without any undesirable thermal effects such as mold damage or inseparable adhesion of the NWs to the mold due to the sacrificial layer.

Generally, the sacrificial layers used in the conventional micro- and nanofabrication[24] are not suitable for large-area nanofabrication because their etching is limited by slow diffusion of etchants in ultrathin etching regions.[25] To allow rapid etching of the sacrificial layer over a large area, we developed the damage process which is performed in the

DOI: 10.1021/acsnano.6b06842
ACS Nano 2017, 11, 1520–1529

middle of the nanotransfer process (Figure 1a (v, vi)). Figure 1b illustrates the damage process in detail. As shown in the left panel in Figure 1b, the as-deposited NW layer has numerous voids and pinholes between grains (see Supporting Information Figure S1). These microscopic voids have been intentionally used in some applications such as nanosieve,[26] because they can easily transport ions, molecules, and liquids. We focused on this intrinsic phenomenon and adapted it to enhance etchant diffusion into the sacrificial layer during the etching process. The tiny voids in the NW layer allow the efficient transport of etchant solution, which selectively reacts with the underlying sacrificial layer. Thus, in the damage process, we partially etch the sacrificial layer by controlling the etching time, and the damage process enables us to obtain a highly porous sacrificial layer while leaving the above NW layer unaffected (Figure 1b (v, vi)). Etchant diffusion is strongly influenced by the porosity of the sacrificial layer, so the sacrificial layer can be fully etched rapidly in the release process even after resin coating is deposited as a flexible template (Figure 1a (vii) and Figure 1b (viii)) because the template resin readily absorbs etchant solution.[27] Finally, we obtain the flexible NW array simply by peeling the flexible template from the master mold (Figure 1a (ix, x)).

To verify the principle of the T-SET process, we investigated the change of etching rate of the sacrificial layer caused by the damage process. We fabricated a Au NW array and underlying nanoscale sacrificial layer of Cr laminated on a hard master mold (see the Experimental Methods). The sample was exposed to the damage process using a diluted Cr etchant for 0, 60, 120, or 180 s. Note that heat treatment was not performed in this experiment to focus on the etching rate of the sacrificial layer. Figure 2a shows scanning electron microscopy (SEM) and optical images of the samples after the damage process was conducted for (i) 0, (ii) 60, (iii) 120, and (iv) 180 s. Although it was difficult to detect obvious changes of the ultrathin sacrificial layer in the cross-sectional SEM images because of their limited resolution (left panels in Figure 2a), notable colorimetric changes were observed in the optical images (right panels in Figure 2a). The changes indicate the continuous damage and removal of the underlying Cr sacrificial layer. As damage time increased, the sacrificial layer changed from dark to light yellow, which means that the only the top Au layer remained. The amount of Cr in the samples (wt %) measured by energy-dispersive X-ray spectroscopy (EDS) decreased continuously with lengthening etchant-assisted damage time, with the Cr content decreasing by more than 30% after 180 s (Figure 2b). This result provides clear evidence of the damage process, in which the Cr etchant penetrated through the pinholes in the upper Au NWs and then partially removed the Cr sacrificial layer. When the damage time was more than 180 s (about 300 s), the sacrificial layer was etched deeply, which induced disordered exfoliation and entanglement of Au NWs on the master mold, as shown in Supporting Information Figure S2.

To further confirm that the sacrificial layer was selectively damaged through the unaffected upper Au NW layer, we measured the surface roughness of Cr sacrificial layers before and after the damage process. These measurements were performed on a flat Au (80 nm)/Cr (30 nm)/Si laminated sample, as illustrated in Figure 2c. Identical samples were treated in the diluted Cr etchant solution for 0 and 180 s, and then the upper Au layer was removed using a selective Au etchant to expose the Cr surface. Figure 2d depicts atomic force microscopy (AFM, XE-100, Park) images of the undamaged (upper panel) and damaged (lowered panel) Cr surfaces. The damage process of the Cr sacrificial layer induced considerable roughness of the Cr surface. The measured 10-point mean roughness R_z, indicating the average of the five highest peaks plus the depth of the five deepest valleys in four different areas (500 × 500 nm), increased from 3.04 to 5.51 nm following the damage process. We also compared the surface roughness of Cr sacrificial and Au NW layers to investigate the selectivity of the damage process for the underlying Cr sacrificial layer, as shown in Figure 2e. The roughness of the underlying Cr surface (red circles) increased as the damage time extended, whereas that of the upper Au layer (blue squares) did not change. These results suggest that the etchant solution penetrated through the pinholes in the upper Au layer and then etched only the underlying sacrificial layer, as proposed in Figure 1b. The same result was obtained for the sacrificial layer on the nanograting master mold (see Supporting Information Figure S3).

Next, we confirmed that the etching rate of the sacrificial layer was definitely enhanced when the whole structure was covered with the flexible template used in the transfer process (Figure 1a (vii, viii)). We used a commercial UV-curable resin containing polyurethane acrylate (PUA) to form the flexible template, as presented in Figure 1a (vii). It should be noted that aqueous solutions could also penetrate the PUA template with high diffusion ability (>10^{-8} m^2/s).[27] The influence of damage time on the final release process was then investigated by dipping the PUA template-covered samples in the diluted Cr etchant (the NW release process in Figure 1a (viii)). The left panels in Figure 2f are cross-sectional SEM images of the samples subjected to different damage times after the release process for 4 h. The nanoscale Cr sacrificial layer was effectively removed because of the prior damage process. The lateral etch depth (etch distance) from the edge of the NW depended on the length of the previous damage process. The right panels in Figure 2f present magnified SEM images of the samples. For the undamaged sample (damage time = 0 s), the etch distance was only a few nanometers. The etch distance increased markedly as the damage time lengthened; etch distances of 8, 30, 60, and 70 nm were observed for the samples with damage times of 0, 60, 10, and 180 s, respectively.

To understand the relationship between the damage process and etchant diffusion, we interpreted the experimental results using the Millington−Quirk model,[28] which describes the diffusion mechanism in a porous medium. According to this model, mass transport strongly depends on the porosity of the medium. The variation of the diffusion coefficient D with porosity is presented in the inset of Figure 2g (the x- and y-axes show the porosity and normalized ratio with D and the nonporous state D_0, respectively). Then, we extracted the experimental D of the etchant solution in the damaged sacrificial layer using the constant D model (Figure 2g).[29] As the damage time extended, the mean D increased from 9.62 × 10^{-14} to 6.68 × 10^{-12} m^2/s, which is an ~70-fold enhancement. This drastic increase of D matches well with the theoretical trend (inset in Figure 2g). This confirms that the etchant solution can diffuse rapidly inside the porous sacrificial layer after the damage process, and the separation of the NW array from the master mold is easily achieved using our T-SET process.

The developed T-SET method was used to transfer a centimeter-scale ultralong Au NW array onto a flexible plastic substrate in a perfectly aligned longitudinal or lateral manner.

DOI: 10.1021/acsnano.6b06842
ACS Nano 2017, 11, 1520−1529

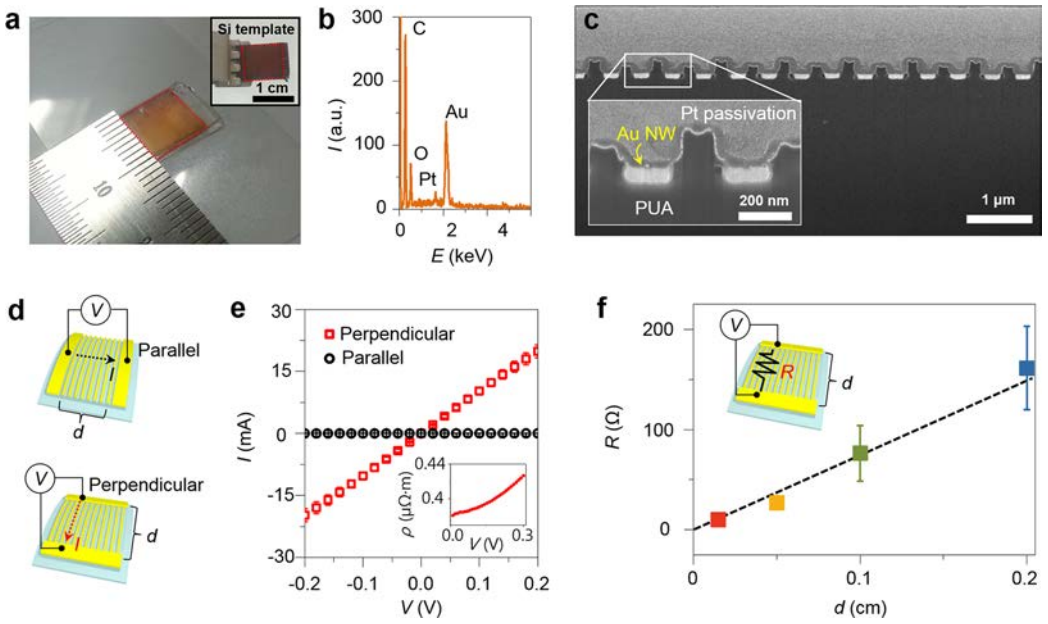

Figure 3. (a) Optical images of transferred Au NW array on flexible-substrate and Si nanograting template after transfer (inset). The transferred region from the template onto the flexible substrate is shown with a red dashed line. (b) EDS material contents of the transferred NW array. (c) Cross-sectional SEM image of the transferred NW array and its magnified image (inset). (d) Schematic illustrations of electrical resistance measurements. (e) Measured electrical current (I) change by the applied voltage (V). Red square and black circle indicate perpendicular and parallel directional results, respectively. Calculated resistivity (ρ) from perpendicular sample is shown in inset. (f) Measured resistance with respect to the perpendicular electrode distances.

Figure 3a shows an optical image of a transferred Au NW array on a flexible substrate. The optically distinct yellow square domains were transferred from the Si master mold (inset in Figure 3a), and neither the transfer template nor the master mold contained substantial residue or defects. Moreover, the EDS data in Figure 3b confirm that no severe material contamination occurred. Top-view SEM images of various regions (see Supporting Information Figure S4) revealed clear line patterns consistent with NWs with extremely high spatial alignment in the lateral direction on the centimeter scale. A cross-sectional SEM image of the transferred sample also confirmed that each NW was perfectly separated, as shown in Figure 3c.

To investigate the alignment of transferred ultralong NWs, we also measured the electrical properties of transferred Au NW arrays using two different electrode designs. One had a parallel electrode configuration along the NW array (upper panel in Figure 3d), and the other had the electrodes positioned perpendicular to the array (lower panel in Figure 3d). Figure 3e depicts the current−voltage (I−V) curves measured using a parameter analyzer (4156C, Agilent). For the perpendicular electrode configuration, the current increased from −19.7 to 19.8 mA as the applied voltage was increased from −0.2 to 0.2 V (red squares in Figure 3e). For the parallel electrode configuration, negligible current (−1.57 to 2.98 pA) was observed in the same voltage range (black circles in Figure 3e). Such anisotropic behavior can be explained by the defectless alignment of the transferred NW array, which allows unidirectional electrical conductivity without any undesired current leakage. Note that the resistivity of the Au NW array calculated from the perpendicular configuration was 400 nΩ·m at 0.2 V (inset in Figure 3d), which is similar to that in previous reports.[30] We also performed I−V measurements using various electrode distances (d) of 150, 500, 1000, and 2000 μm; the measured resistances are plotted in the inset of Figure 3f. As d increased, resistance increased linearly, which implies that the aligned NW arrays were stably transferred over an ultralong length with notable uniformity.

So far, it has been shown that the developed T-SET process facilitating the ultralong Au NW transfer with centimeter scale. The most important advantage of this method is the possibility for various PVD-formed NWs to transfer with enhanced material properties. Microscopic pores are a natural outcome of the PVD-formed NWs, irrespective of the fabrication methods, such as evaporation and sputtering,[31,32] and they can be easily controlled by adjusting PVD conditions,[33,34] such as deposition angle, chamber pressure, and chamber temperature. Moreover, the physically and chemically separated NW and master mold by a sacrificial layer enable us to apply the additional high-temperature thermal annealing to induce crystallization of the NW, which has not been achieved using conventional mold-based nanotransfer methods. Thus, it is possible to transfer various materials as quality-enhanced NWs on a flexible template with our method, by means of selecting an appropriate sacrificial layer, which has a high melting point, low diffusability into the NW and master mold, and selective reactivity with a proper etchant solution.

To exemplify the applicability of the proposed method for various material transfer with high-temperature capability, we selected $BaTiO_3$, which shows piezoelectric, pyroelectric, and ferroelectric characteristics that depend on its degree of crystallinity.[35] As a sacrificial layer, the Cr was used because it has a significantly low solid-phase diffusion coefficient[36] based on its high melting point (1907 °C). The process began with the sequential deposition of a sacrificial Cr layer and $BaTiO_3$ NWs layer followed by high-temperature crystallization at 700 °C and then the damage process (see Experimental Methods section). The annealing could enlarge the nanoscale grain size to microscale, reducing the porosity, and it prevents the damage process. It is possible to achieve the crystallinity improvement

DOI: 10.1021/acsnano.6b06842
ACS Nano 2017, 11, 1520−1529

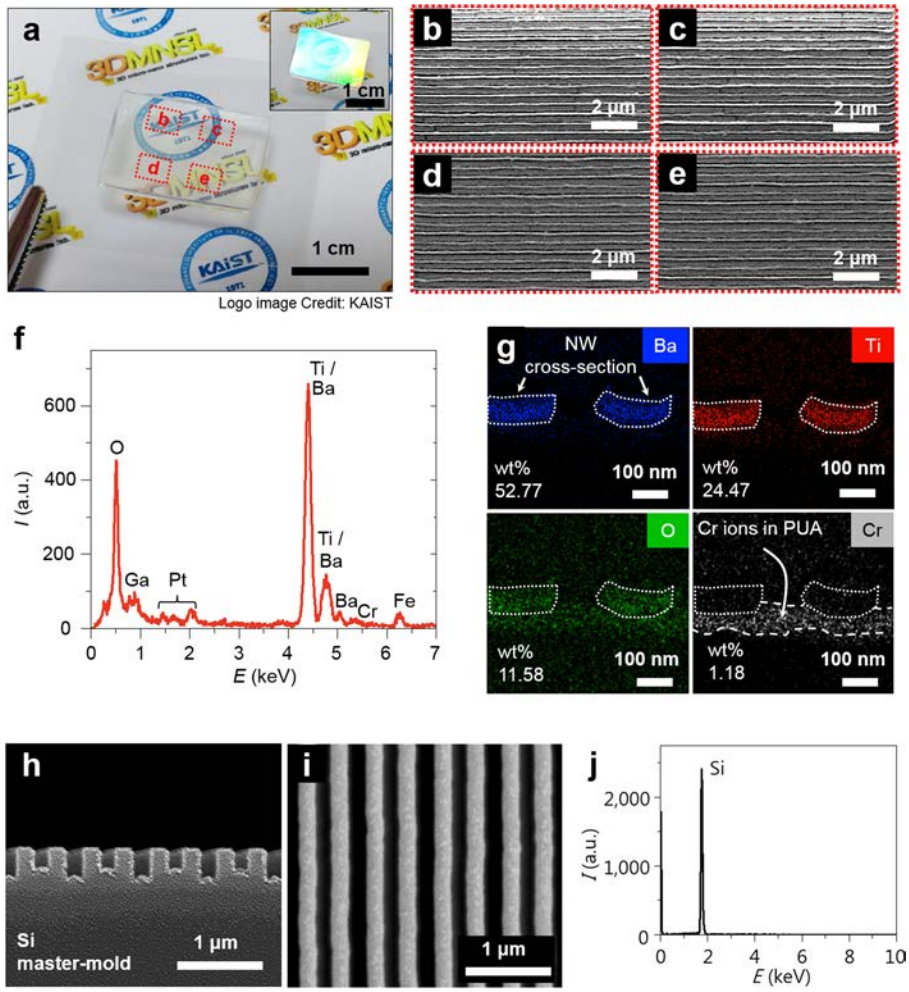

Figure 4. (a) Optical image of transferred $BaTiO_3$ NW array on flexible substrate (logo images are used with permission from KAIST and 3DMNSL). (b–e) SEM images observed from the four different areas marked in (a). (f) EDS element data measured from cross-sectional face of transferred NWs. (g) EDS mapping data and their weight %. The cross-sectional area of NW is indicated with a white short-dashed line, and the trapped Cr ions in the PUA is indicated with a white long-dashed line. (h, i) Cross-sectional (i) and top (h) SEM images of Si nanograting master mold after the whole process. (j) EDS content analysis of the master mold.

with maintaining the nanoscale porosity and grain boundaries in the used rapid annealing condition[37] below half of the T_m. Therefore, the proposed damage process cannot be affected by the prethermal annealing process (see Supporting Information Figure S5). During the fabrication process, X-ray diffraction (XRD) analysis was conducted to verify the change in crystallinity of the $BaTiO_3$ NWs. The XRD data confirmed that the $BaTiO_3$ crystallinity was enhanced even after the damage process of the sacrificial layer (see Supporting Information Figure S6). Note that the strong adhesion between the NWs and master mold typically induced by high-temperature crystallization is not an issue in our T-SET method because the NWs can be easily separated from the master mold following high-temperature crystallization by the developed sacrificial-layer removal method.

Figure 4a presents an optical image of a transferred $BaTiO_3$ NW array on a flexible plastic substrate. The nanoscale thickness of the $BaTiO_3$ NWs (80 nm) means the flexible piezoelectric array is highly transparent under visible light. The NWs displayed a uniform green Bragg diffraction, indicating their high spatial alignment (inset in Figure 3a). The SEM images captured in the upper left and right and lower left and right areas of the sample (Figure 3b–e, respectively) contain well-defined uniform line nanopatterns. This confirms that perfectly aligned centimeter-scale $BaTiO_3$ NWs were successfully transferred without causing defects and degradation. To evaluate the transfer of the NW array over a large area, we analyzed hundreds of consecutive points using SEM. The results indicated that more than a 450 μm length $BaTiO_3$ NW array was transferred continuously onto the flexible substrate (see Movie S1 in the Supporting Information). In this experiment, the transfer was conducted with the centimeter-scale Si master mold because of the experimental conditions, such as laboratory-level lithography and PVD systems, but the developed method, based on a well-established top-down approach, is employed for the larger area NW fabrication with a larger master mold up to wafer scale. Although a few cracks appeared in the NWs because of the induced stress concentration during the peel-off step, they should be prevented by optimizing the transfer conditions.[38] We analyzed the influence of the Cr etchant solution-involved damage, and the release processes on the $BaTiO_3$ and verified that the fabricated NWs are not degraded during the transfer fabrication by the chemical solution (see Supporting Information Figure

DOI: 10.1021/acsnano.6b06842
ACS Nano 2017, 11, 1520–1529

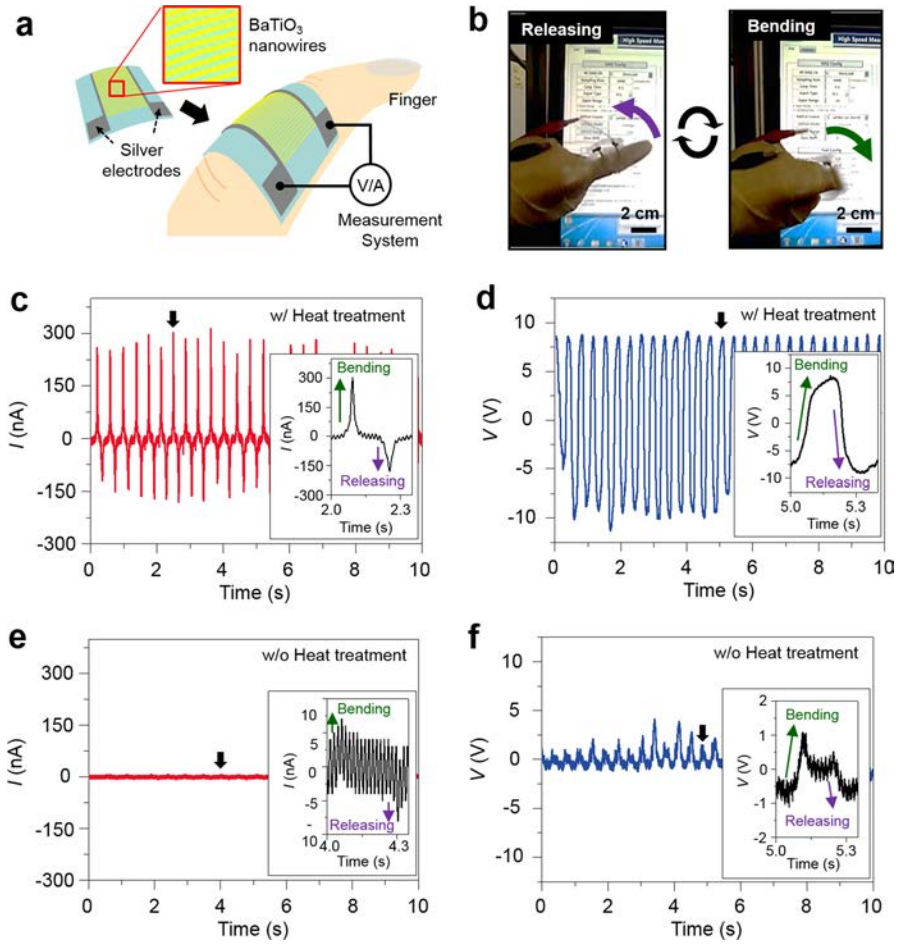

Figure 5. (a) Schematic illustration of electrical measurement of transferred $BaTiO_3$ NW array. Silver electrodes were formed on the NW array with the perpendicular direction. (b) Optical images of the attached flexible device on the index finger. (c–f) Measured short circuit current (I) (c,e) and open circuit voltage (V) (d,f). Significantly enhanced electrical signals were measured from the crystallized NW array device (I = ~300 nA and V = ~10 V in c and d, respectively), contrasting to the amorphous NW array device (I = ~8 nA and V = ~2 V in e and f, respectively).

S7). We also performed the transfer process using samples subjected to different damage times (0 and 300 s). These samples did not show a successful transfer of NW arrays. Few NWs were transferred onto the flexible template because of the slow etching of the sacrificial layer in the undamaged sample. Meanwhile, a tangled NW array was transferred from the sample with a damage time of 300 s because the extended damage process had already released some NWs (see Supporting Information Figure S8).

Although the crystallinity of $BaTiO_3$ was enhanced by heat treatment at 700 °C, this high-temperature process could potentially also generate alloys or induce migration in the Cr sacrificial layer. Therefore, it was necessary to determine the material composition of the crystallized $BaTiO_3$ NWs. We performed EDS elemental mapping analysis of a transferred $BaTiO_3$ NW array on a flexible substrate. To allow accurate analyses, EDS data were obtained from the cross-sectional face of the transferred $BaTiO_3$ NWs cut by a focused ion beam. Figure 4f,g shows the measured EDS elements and relevant mapping data, respectively (detailed elemental data are provided in Supporting Information Table S1). The crowded barium (Ba, blue dots), titanium (Ti, red dots), oxygen (O, green dots), and Cr (yellow dots) maps and the related mass percentages enabled us to analyze the elemental locations and material composition of the sample. The mapping data indicated that the transferred sample was mainly composed of Ba, Ti, and O with contents of 52.77, 24.47 , and 11. 58 wt %, respectively. The NWs were almost entirely composed of Ba, Ti, and O. The small amount of Cr (1.18 wt %) was detected in the PUA. During the NWs release process, the Cr sacrificial layer is dissolved in the etchant solution, which penetrated through the PUA covering the NWs and Si master-mold, and then, the ionized Cr ions are diffused out through the PUA layer. In this process, few Cr ions are trapped in the PUA. Moreover, we also performed SEM and EDS analyses of the used Si master mold. To clean the master mold, we performed the standard piranha cleaning and diluted hydrofluoric acid dipping for 10 min and 30 s, respectively, after the transfer process. Neither marked physical damage nor chemical contamination in the master mold was detected in cross-sectional and top-view SEM images (Figure 4h,i) or EDS data (Figure 4j), respectively. These results indicate that we can recycle the Si master mold repeatedly, which makes our developed process more cost-effective.

The effect of heat treatment on the fabricated $BaTiO_3$ NWs was investigated by measurement of their piezoelectric signal. To measure the piezoelectric output of the $BaTiO_3$ NWs, we fabricated a flexible nanogenerator using the transferred NW

DOI: 10.1021/acsnano.6b06842
ACS Nano 2017, 11, 1520–1529

array. Silver electrodes were deposited on two ends of the transferred NW array (defined NW length by width = 2 × 1.5 cm) with a perpendicular electrode configuration, as shown in Figure 5a. The nanoarray-based nanogenerator was mechanically very flexible and could be bent and released smoothly on the joint of an index finger (Figure 5a,b). The electrical output signal was measured in real time using a programmable electrometer (Keithley 6514) (Figure 5c,d). We also performed the same experiment using an amorphous $BaTiO_3$ (a-$BaTiO_3$) NW array fabricated on a flexible substrate without high-temperature crystallization (Figure 5e, f) to ensure that the measured electrical signal was affected by the degree of crystallinity of $BaTiO_3$. During repeated bending and releasing motions (~2.5 Hz), the well-crystallized $BaTiO_3$ NW array nanogenerator produced a short-circuit current and open-circuit voltage of up to ~300 nA and ~10 V, respectively (Figure 5c,d). In contrast, the a-$BaTiO_3$ NW-based device produced much smaller output signals of about ~8 nA and ~1 V (Figure 5e,f). The real-time piezoelectric output signals of our centimeter-scale $BaTiO_3$ NW-based nanogenerator are presented in Supporting Information Movie S2. These dramatic piezoelectric changes indicate that the thermal crystallization performed at 700 °C in the T-SET method increased the crystallinity of the $BaTiO_3$ NWs, and their crystalline structure was maintained after the transfer process. We also compared the output performance of our developed nanogenerators and that of other $BaTiO_3$ based nanogenerators (see Supporting Information Table S2). It shows that our fabricated flexible nanogenerator generates a higher level of voltage and current from the biomechanical energy because the structurally superior and heat-treated NWs array was successfully fabricated on the centimeter-scale flexible template without material degradations.

CONCLUSIONS

In summary, we demonstrated a versatile transfer method for NWs to obtain ultralong, large-area, and perfectly aligned configurations on flexible plastic substrates. Importantly, this method tolerated high-temperature processes to achieve excellent material functionality. This simple transfer approach, which is called the T-SET method, is based on a developed damage process of a sacrificial layer, which facilitates rapid removal of the nanometer-thick sacrificial layer in the final release process. Without this crucial damage process, the sacrificial layer etching is extremely slow because of the restricted diffusion of the etchant. Using the T-SET method, we obtained an ultralong, dense, perfectly laterally aligned, centimeter-scale Au NW array on a flexible plastic substrate. This technology also enabled us to perform high-temperature thermal treatment to induce crystallization, which is essential to improve the material properties of NWs, without any material contamination or adhesion issues. Consequently, we realized an ultralong, perfectly aligned, ceramic NW array consisting of polycrystalline $BaTiO_3$ that was crystallized at high temperature and then transferred onto a flexible plastic substrate. In addition, a piezoelectric flexible nanogenerator fabricated from the centimeter-scale aligned $BaTiO_3$ NWs harvested biomechanical energy to produce electrical energy of up to 300 nA and 10 V. The performance of the nanogenerator was enhanced by the improved crystallinity of the NWs following heat treatment. We expect that our developed T-SET process can be extended to various wearable and flexible electronics such as sensors, transistors, and displays with various ceramic and semiconductor NWs. Moreover, this nanofabrication method can also be adapted to three-dimensional nanofabrication to produce state-of-the-art nanochannel and nanoelectromechanical systems.

EXPERIMENTAL METHODS

T-SET Verification Experiment. Chromium (Cr; 30 nm) and gold (Au; 80 nm) layers were thermally deposited, using a thermal evaporator (Korea vacuum tech.), on a prefabricated Si nanograting master mold (pitch: 400 nm, line width: 150 nm, line space: 250 nm) as the sacrificial layer and NWs, respectively. The fabrication of the nanograting master mold is described in a previous report. The damage process, conducted on both the Au/Cr deposited nanograting and flat substrates, is performed using 10:1 diluted Cr etchant (CE-905N, Transene Company, Inc.). After the damage process, the specimens were rinsed with deionized (DI) water for 5 min to reduce the chemical solution residue. To measure the Cr roughness, Au strip is performed on the flat sample using 10:1 diluted Au etchant for 120 s after the damage process. Then, a commercial UV-curable resin containing polyurethane acrylate (PUA; HC11M-J5, Minuta Technology Co., Ltd.) was used for the flexible template by 200 mJ G-line UV exposure. Finally, the enhanced sacrificial layer etching was verified through the dipping of the PUA template-covered nanograting samples in 5:1 diluted Cr etchant, and then, the specimens were rinsed again by deionized (DI) water for 5 min.

Gold Nanowire Array Transfer. The "transfer" process starts with the fabrication of Au NWs and Cr sacrificial-layer deposition on a Si nanograting master mold, as we described above. After the deposition, we performed surface cleaning (1 min plasma cleaning under oxygen base) on the specimen. Then the damage-process on sacrificial layer is conducted using 10:1 diluted Cr etchant (CE-905N, Transene Company, Inc.) for 180 s. A commercial UV curable polyurethane-acrylate PUA (HC11M-J5, Minuta Technology Co., Ltd.) is deposited on the specimen, and a commercial 100 μm-thick polyethylene-terephthalate PET film is covered on the PUA deposited template. The multistacked sample is exposed to UV exposure system (MJB4, SÜSS Micro Tec.) with 100 mJ (365 nm wavelength). The release process is performed by dipping the sample in a 5:1 diluted Cr etchant solution (CE905N, Transene Company, Inc.) for 5 h. After the Cr etchant solution treatments, including the damage and release processes, the specimen is treated with a DI water rinse process for cleaning. Finally, the PET film is peeled off gently to transfer the NW array to the flexible substrate.

$BaTiO_3$ Nanowire Array Transfer. $BaTiO_3$ NW array transfer also begins with a 30 nm Cr sacrificial layer and 80 nm amorphous barium-titanate ($BaTiO_3$) NW material deposition. Cr and $BaTiO_3$ are deposited using a thermal evaporator and RF sputtering system, respectively. Then the high-temperature heat treatment is followed using a vertical vacuum furnace (P&Tech.) under a 700 °C oxygen atmosphere for 20 min (ramping rate is 8 °C per a minute and cooling rate is 3 °C per a minute). After the RTA process, the damage (10:1 diluted Cr etchant for 180 s), flexible-plastic substrate formation, and release processes (5:1 diluted Cr etchant for 5 h), which is same process and condition as the Au NW array transfer above), are performed sequentially. After the Cr etchant solution treatments, including the damage and release processes, the specimen is treated with a DI water rinse process for cleaning. Finally, the PET film is peeled off gently to transfer NW array to the flexible substrate.

ASSOCIATED CONTENT

Supporting Information

The Supporting Information is available free of charge on the ACS Publications website at DOI: 10.1021/acsnano.6b06842.

Figure S1: Pin-hole inspection of deposited gold and barium titanate NWs by SEM. Figure S2: Optical images by damaging time variation. Figure S3: SEM images of the NWs deposited master-mold after damage process.

DOI: 10.1021/acsnano.6b06842
ACS Nano 2017, 11, 1520–1529

Figure S4: SEM images of transferred gold NW array. Figure S5: $BaTiO_3$ morphology change by heat treatment. Figure S6: XRD pattern changes of barium titanate after the 700 °C annealing. Figure S7: Influences of Cr etchant solution on Barium titanate (PDF) Figure S8: $BaTiO_3$ transfer results from various damage process conditions. Table S1: EDS element analysis of the transferred $BaTiO_3$ NWs. Table S2: Structural characteristics and electrical output performance of various $BaTiO_3$-based nanogenerators (PDF)
Movie S1: Ultralong and seamless $BaTiO_3$ NW array on a flexible substrate (AVI)
Movie S2: Short-circuit current and open circuit-voltage output of the fabricated flexible nanogenerator (AVI)

AUTHOR INFORMATION

Corresponding Author

*E-mail: jbyoon@kaist.ac.kr.

ORCID

Jun-Bo Yoon: 0000-0002-9447-3807

Present Address

‖Samsung Electronics, Samsungjeonja-ro, Hwaseong, Gyeonggi-do 445-330, Republic of Korea

Notes

The authors declare no competing financial interest.

ACKNOWLEDGMENTS

This work was supported by a National Research Foundation of Korea (NRF) grant funded by the Korean government (MEST) (no. 2011-0028781)

REFERENCES

(1) Cao, G.; Wang, Y. *Nanostructures and Nanomaterials, Synthesis, Properties and Applications*; Imperial College Press: London, 2011.
(2) Liu, X.; Long, Y. Z.; Liao, L.; Duan, X.; Fan, Z. Large-Scale Integration of Semiconductor Nanowires for High-Performance Flexible Electronics. *ACS Nano* **2012**, *6*, 1888−1900.
(3) Lee, P.; Lee, J.; Lee, H.; Yeo, J.; Hong, S.; Nam, K. H.; Lee, D.; Lee, S. S.; Ko, S. H. Highly Stretchable and Highly Conductive Metal Electrode by Very Long Metal Nanowire Percolation Network. *Adv. Mater.* **2012**, *24*, 3326−3332.
(4) Amjadi, M.; Pichitpajongkit, A.; Lee, S.; Ryu, S.; Park, I. Highly Stretchable and Sensitive Strain Sensor Based on Silver Nanowire-Elastomer Nanocomposite. *ACS Nano* **2014**, *8*, 5154−5163.
(5) Yeon, J.; Lee, Y. J.; Yoo, D. E.; Yoo, K. J.; Kim, J. S.; Lee, J.; Lee, J. O.; Choi, S. J.; Yoon, G. W.; Lee, D. W.; Lee, G. S.; Hwang, H. C.; Yoon, J.-B. High Throughput Ultralong (20 Cm) Nanowire Fabrication Using a Wafer-Scale Nanograting Template. *Nano Lett.* **2013**, *13*, 3978−3984.
(6) Liu, X.; Gu, L.; Zhang, Q.; Wu, J.; Long, Y.; Fan, Z. All-Printable Band-Edge Modulated ZnO Nanowire Photodetectors with Ultra-High Detectivity. *Nat. Commun.* **2014**, *5*, 4007.
(7) Xu, C.; Li, Z.; Yang, C.; Zou, P.; Xie, B.; Lin, Z.; Zhang, Z.; Li, B.; Kang, F.; Wong, C.-P. An Ultralong, Highly Oriented Nickel-Nanowire-Array Electrode Scaffold for High-Performance Compressible Pseudocapacitors. *Adv. Mater.* **2016**, *28*, 5777.
(8) Wang, Q.; Li, J.; Lei, Y.; Wen, Y.; Wang, Z.; Zhan, X.; Wang, F.; Wang, F.; Huang, Y.; Xu, K.; He, J. Oriented Growth of Pb 1− X Sn X Te Nanowire Arrays for Integration of Flexible Infrared Detectors. *Adv. Mater.* **2016**, *28*, 3596−3601.
(9) Duan, X.; Lieber, C. M. General Synthesis of Compound Semiconductor Nanowires. *Adv. Mater.* **2000**, *12*, 298−302.
(10) Tan, E. P. S.; Zhu, Y.; Yu, T.; Dai, L.; Sow, C. H.; Tan, V. B. C.; Lim, C. T. Crystallinity and Surface Effects on Young's Modulus of CuO Nanowires. *Appl. Phys. Lett.* **2007**, *90*, 163112.
(11) Ahn, M.-W.; Park, K.-S.; Heo, J.-H.; Park, J.-G.; Kim, D.-W.; Choi, K. J.; Lee, J.-H.; Hong, S.-H. Gas Sensing Properties of Defect-Controlled ZnO-Nanowire Gas Sensor. *Appl. Phys. Lett.* **2008**, *93*, 263103.
(12) He, X.; Gao, W.; Xie, L.; Li, B.; Zhang, Q.; Lei, S.; Robinson, J. M.; Hároz, E. H.; Doorn, S. K.; Wang, W.; Vajtai, R.; Ajayan, P. M.; Adams, W. W.; Hauge, R. H.; Kono, J. Wafer-Scale Monodomain Films of Spontaneously Aligned Single-Walled Carbon Nanotubes. *Nat. Nanotechnol.* **2016**, *11*, 633−638.
(13) Geier, M. L.; McMorrow, J. J.; Xu, W.; Zhu, J.; Kim, C. H.; Marks, T. J.; Hersam, M. C. Solution-Processed Carbon Nanotube Thin-Film Complementary Static Random Access Memory. *Nat. Nanotechnol.* **2015**, *10*, 944−948.
(14) Nguyen, T. D.; Nagarah, J. M.; Qi, Y.; Nonnenmann, S. S.; Morozov, A. V.; Li, S.; Arnold, C. B.; McAlpine, M. C. Wafer-Scale Nanopatterning and Translation into High-Performance Piezoelectric Nanowires. *Nano Lett.* **2010**, *10*, 4595−4599.
(15) Qi, Y.; Jafferis, N. T.; Lyons, K.; Lee, C. M.; Ahmad, H.; McAlpine, M. C. Piezoelectric Ribbons Printed onto Rubber for Flexible Energy Conversion. *Nano Lett.* **2010**, *10*, 524−528.
(16) McAlpine, M. C.; Ahmad, H.; Wang, D.; Heath, J. R. Highly Ordered Nanowire Arrays on Plastic Substrates for Ultrasensitive Flexible Chemical Sensors. *Nat. Mater.* **2007**, *6*, 379−384.
(17) Zaumseil, J.; Meitl, M. A.; Hsu, J. W. P.; Acharya, B. R.; Baldwin, K. W.; Loo, Y.-L.; Rogers, J. A. Three-Dimensional and Multilayer Nanostructures Formed by Nanotransfer Printing. *Nano Lett.* **2003**, *3*, 1223−1227.
(18) Pak, Y.; Lim, N.; Kumaresan, Y.; Lee, R.; Kim, K.; Kim, T. H.; Kim, S.-M.; Kim, J. T.; Lee, H.; Ham, M.; Jung, G.-Y. Palladium Nanoribbon Array for Fast Hydrogen Gas Sensing with Ultrahigh Sensitivity. *Adv. Mater.* **2015**, *27*, 6945−6952.
(19) Park, K.-I.; Xu, S.; Liu, Y.; Hwang, G.-T.; Kang, S.-J. L.; Wang, Z. L.; Lee, K. J. Piezoelectric BaTiO 3 Thin Film Nanogenerator on Plastic Substrates. *Nano Lett.* **2010**, *10*, 4939−4943.
(20) Doyle, C. D. Estimating Thermal Stability of Experimental Polymers by Empirical Thermogravimetric *Analysis*. *Anal. Chem.* **1961**, *33*, 77−79.
(21) Dauskardt, R. H.; Lane, M.; Ma, Q.; Krishna, N. Adhesion and Debonding of Multi-Layer Thin Film Structures. *Eng. Fract. Mech.* **1998**, *61*, 141−162.
(22) Kim, K.; Rho, Y.; Kim, Y.; Kim, S. H.; Hahm, S. G.; Park, C. E. A Lattice-Strained Organic Single-Crystal Nanowire Array Fabricated *via* Solution-Phase Nanograting-Assisted Pattern Transfer for Use in High-Mobility Organic Field-Effect Transistors. *Adv. Mater.* **2016**, *28*, 3209−3215.
(23) Sun, Z.; Chen, Z.; Zhang, W.; Choi, J.; Huang, C.; Jeong, G.; Coughlin, E. B.; Hsu, Y.; Yang, X.; Lee, K. Y.; Kuo, D. S.; Xiao, S.; Russell, T. P. Directed Self-Assembly of Poly(2-Vinylpyridine)- B -Polystyrene- B -poly(2-Vinylpyridine) Triblock Copolymer with Sub-15 Nm Spacing Line Patterns Using a Nanoimprinted Photoresist Template. *Adv. Mater.* **2015**, *27*, 4364−4370.
(24) Kim, K. S.; Zhao, Y.; Jang, H.; Lee, S. Y.; Kim, J. M.; Kim, K. S.; Ahn, J.-H.; Kim, P.; Choi, J.-Y.; Hong, B. H. Large-Scale Pattern Growth of Graphene Films for Stretchable Transparent Electrodes. *Nature* **2009**, *457*, 706−710.
(25) Sparreboom, W.; Eijkel, J. C. T.; Bomer, J.; van den Berg, A. Rapid Sacrificial Layer Etching for the Fabrication of Nanochannels with Integrated Metal Electrodes. *Lab Chip* **2008**, *8*, 402.
(26) Choi, D.-H.; Han, Y. D.; Lee, B.-K.; Choi, S.-J.; Yoon, H. C.; Lee, D.-S.; Yoon, J.-B. Use of a Columnar Metal Thin Film as a Nanosieve with Sub-10 Nm Pores. *Adv. Mater.* **2012**, *24*, 4408−4413.
(27) Huacuja-Sánchez, J. E.; Müller, K.; Possart, W. Water Diffusion in a Crosslinked Polyether-Based Polyurethane Adhesive. *Int. J. Adhes. Adhes.* **2016**, *66*, 167−175.
(28) Millington, R. J.; Quirk, J. P. Permeability of Porous Solids. *Trans. Faraday Soc.* **1961**, *57*, 1200.

DOI: 10.1021/acsnano.6b06842
ACS Nano 2017, 11, 1520−1529

(29) Bühler, J.; Steiner, F.-P.; Baltes, H. Silicon Dioxide Sacrificial Layer Etching in Surface Micromachining. *J. Micromechanics Microengineering* **1997**, *7*, R1−R13.
(30) Bietsch, A.; Michel, B. Size and Grain-Boundary Effects of a Gold Nanowire Measured by Conducting Atomic Force Microscopy. *Appl. Phys. Lett.* **2002**, *80*, 3346.
(31) Nakahara, S. Microporosity in Thin Films. *Thin Solid Films* **1979**, *64*, 149−161.
(32) Nakahara, S. Microporosity Induced by Nucleation and Growth Processes in Crystalline and Non-crystalline Films. *Thin Solid Films* **1977**, *45*, 421−432.
(33) Robbie, K.; Sit, J. C.; Brett, M. J. Advanced Techniques for Glancing Angle Deposition. *J. Vac. Sci. Technol., B: Microelectron. Process. Phenom.* **1998**, *16*, 1115−1122.
(34) Seshan, K. *Handbook of Thin Film Deposition Processes and Techniques*; William Andrew Publishing: New York, 2001.
(35) Jaffe, B.; Cook, W.; Jaffe, H. *Piezoelectric Ceramics*; Academic Press: London, 1971.
(36) Miyoshi, S.; Martin, M. B. Site Cation Diffusivity of Mn and Cr in Perovskite-type LaMnO3 with Cation Deficit Nonstoichiometry. *Phys. Chem. Chem. Phys.* **2009**, *11*, 3063−3070.
(37) Verhoeven, J. D. *Fundamentals of Physical Metallurgy*, 2nd ed.; John Wiley & Sons, Inc.: New York, 1975.
(38) Kanninen, M. F. An Augmented Double Cantilever Beam Model for Studying Crack Propagation and Arrest. *Int. J. Fract.* **1973**, *9*, 83−91.

DOI: 10.1021/acsnano.6b06842
ACS Nano 2017, 11, 1520−1529